Article | Received 6 September 2025; Revised 24 October 2025; Accepted 6 November 2025; Published 12 November 2025
https://doi.org/10.55092/sc20250028

Research on intelligent analysis method for dynamic response of onshore wind turbines

Maolin Dai[1], Liang Cao[2,3,4,*], Guoqing Huang[1], Xuhong Zhou[1,2] and Jiepeng Liu[1]

[1] School of Civil Engineering, Chongqing University, Chongqing 400045, China
[2] College of Civil Engineering, Hunan University, Changsha 410082, China
[3] Key Laboratory for Damage Diagnosis of Engineering Structures of Hunan Province, Hunan University, Changsha 410082, China
[4] National Key Laboratory of Bridge Safety and Resilience, Changsha 410082, China

* Correspondence author; E-mail: liangcao@hnu.edu.cn.

Highlights:

- A 13-DOF nonlinear multibody model is developed, incorporating coupled tower-blade-nacelle-rotor dynamics and often-neglected tower torsion.
- An intelligent mode selection algorithm is proposed to optimize vibration mode functions, balancing computational efficiency with simulation accuracy.
- Validation against OpenFAST shows relative errors within 3.5% for key responses, enabling reliable structural assessment and future optimization.

Abstract: This paper introduces a high-fidelity, nonlinear dynamic modeling and intelligent analysis framework for assessing the dynamic response of onshore wind turbines. A 13-degree-of-freedom (DOF) multibody model is established using Euler-Lagrange formalism, integrating coupled rigid and flexible body dynamics across the tower, blades, rotor, nacelle, and drivetrain. The tower and blades are modeled as Euler-Bernoulli beams capable of capturing both bending and torsional deformation, with aerodynamic loads computed via an enhanced blade element momentum (BEM) approach. To ensure predictive accuracy under complex loading conditions, an intelligent analysis algorithm is developed for selection and validation of vibration mode functions based on structural response convergence. Numerical simulations, implemented symbolically in MATLAB®, are validated against the widely recognized OpenFAST code. Results indicate that the proposed model effectively captures nonlinear and coupled dynamic turbine behavior, achieving relative errors within 3.5% in key response metrics. The framework offers a reliable tool for structural dynamic assessment and establishes a foundation for future applications in optimization and control of large-scale wind energy systems.

Keywords: onshore wind turbine; nonlinear dynamics; flexible multibody system; modal decomposition; intelligent mode selection; aerodynamic coupling; structural response simulation

1. Introduction

Driven by escalating global demand for sustainable energy infrastructure, wind power has become a cornerstone of the renewable energy transition, offering significant benefits such as carbon-neutral operation, environmental stewardship, operational reliability, and high energy conversion efficiency [1,2]. As one of the most commercially mature and rapidly expanding renewable energy technologies, wind power capacity has demonstrated characteristic exponential growth. According to the Global Wind Report 2025 [3], the sector experienced unprecedented expansion in 2024, with 117 gigawatts (GW) of new installations worldwide. Furthermore, the market is projected to maintain a compound annual growth rate (CAGR) of 8.8% through 2030.

Wind turbine towers [4,5], a principal component of onshore wind turbines, serve two critical structural and aerodynamic roles, making them essential to the overall effectiveness and safety of wind energy systems. First, they elevate the rotor blades to heights where wind speeds are more favorable due to the vertical wind shear effect, thereby improving aerodynamic efficiency and energy capture. Second, they function as the primary load-bearing structures, supporting the nacelle, hub, and rotor assemblies while transmitting complex dynamic loads-including gravitational, aerodynamic, inertial, and operational loads-to the foundation. These dual functions require towers to possess high bending stiffness, adequate buckling resistance, and favorable vibrational characteristics. The natural frequency of the tower must be carefully designed to avoid resonance with rotor excitation frequencies (typically 1P and 3P), which can lead to amplified structural responses and potential fatigue failure. A tower that is either too stiff or too flexible may result in adverse effects such as excessive blade tip deflection, reduced energy production due to misalignment, and long-term material degradation. Moreover, environmental factors such as turbulence intensity, extreme gusts, and seismic loading necessitate towers that are not only strong but also dynamically resilient. Cost analyses indicate that tower manufacturing accounts for approximately 14%–20% of the capital expenditure for onshore wind projects [6]. This economic reality underscores the need for a comprehensive design methodology that integrates structural safety with cost efficiency-balancing fatigue endurance, buckling resistance, vibration suppression, and mass minimization within a multi-objective optimization framework.

To achieve this, modern computational optimization of wind turbine towers typically integrates two modules: (1) a high-fidelity structural analysis model that captures key physical responses, and (2) a numerical optimization engine that navigates the complex design space under multiple constraints. The structural analysis component serves as the predictive core, tasked with evaluating the tower's mechanical behavior under both operational and extreme loading conditions. Two mainstream analytical approaches are widely employed. The first is based on Euler-Bernoulli beam theory [7–9], in which the tower is idealized as a slender beam and discretized using one-dimensional beam elements. This method is computationally efficient and reasonably captures global bending, axial, and shear deformations, making it suitable for preliminary design and parametric studies. The second, more detailed approach employs three-dimensional finite element analysis (FEA) [10–12], using shell or solid (brick) elements to model the tower geometry and material behavior. FEA provides localized stress resolution, captures geometric nonlinearity, and accommodates complex boundary conditions, making it ideal for high-fidelity simulations and failure assessments. Within the optimization module, gradient-based algorithms, evolutionary strategies (e.g., genetic algorithms), or surrogate-assisted

methods are used to identify optimal tower geometries and material layouts that minimize mass or cost while satisfying constraints on stress, displacement, buckling safety factors, and modal frequencies. The coupling of structural fidelity and algorithmic robustness forms the foundation for automated, performance-driven wind turbine tower design, enabling the development of lighter, safer, and more economically competitive renewable energy infrastructure.

However, to comprehensively capture the dynamic behavior of onshore wind turbines-particularly under operational and extreme loading scenarios-it is essential to adopt an integrated analysis framework that accounts for full system interactions and inherent nonlinearities. To enhance modeling accuracy and predictive capability, this study employs a multi-body dynamics (MBD) approach [13–15]. The analysis begins with the formulation of the kinematics for both rigid and flexible bodies, followed by the derivation of coupled equations of motion that describe the interactions between rigid-body dynamics and elastic deformations. While high-fidelity commercial tools offer comprehensive nonlinear capabilities, they often entail significant computational cost. The proposed framework seeks a balance by implementing a concise yet nonlinear multibody formulation that efficiently accounts for finite rigid-body rotations and large elastic displacements, providing a physically consistent representation suitable for rapid dynamic analysis and design optimization. While Timoshenko beam effects may become significant for larger-scale turbines, the nonlinear Euler-Bernoulli beam theory is employed here to capture the tower's structural flexibility, allowing the elastic rotation matrix to reflect large deformations and torsional effects. Additionally, balancing computational efficiency with accuracy, an intelligent optimization algorithm was employed to develop a method for identifying vibration mode functions applicable to towers and blades of various structural forms.

2. Mechanical modelling of the 13-DOF OWT system

A comprehensive 13-degree-of-freedom (13-DOF) model for an onshore wind turbine (OWT) is developed based on the Euler-Lagrange formalism. This model utilizes a hybrid multibody and modal-based formulation to systematically describe the system's kinetic and potential energies. It captures the fully coupled dynamics of the blades, rotor, nacelle, and tower, with particular emphasis on explicitly incorporating the tower's torsional degree of freedom-an aspect often neglected in conventional modeling approaches. Nonlinear aeroelastic effects are represented through the modal decomposition of blade deformation, and the influence of collective blade pitch control is rigorously integrated into the framework. This advanced modeling strategy provides a robust and physically consistent foundation for analyzing the dynamic response of onshore wind turbines under a wide range of operational scenarios.

2.1. Model overview

The degrees of freedom (DOFs) and coordinate systems (CSs) of the OWT model are depicted in Figure 1. Tower deformations are expressed in the global inertial coordinate system (OXYZ, referred to as Frame $\mathcal{F}_O$), with its origin located at the tower base. The nacelle and rotor motions are described in a local moving coordinate system ($o_t x_t y_t z_t$, denoted as Frame $\mathcal{F}_T$), with its origin fixed at the center of the tower top. Each blade has its own local rotating coordinate system ($o_r x_{ba} y_{ba} z_{ba}$, denoted as Frame $\mathcal{F}_{ba}$, a = 1, 2, 3), originating at the rotor center.

The blades and tower are modeled as Euler-Bernoulli beams. As illustrated in Figure 1, each blade [16] exhibits two deformation DOFs-$u_{ba}(r_b, t)$ and $v_{ba}(r_b, t)$ (a = 1, 2, 3), representing flapwise and edgewise displacements, respectively. Tower motion is characterized by the translational DOFs $u_t(z, t)$ and $v_t(z, t)$, corresponding to fore-aft and side-to-side vibrations, along with the torsional DOF $\varphi_t(z, t)$. The torsional moment at the tower top often governs the design of the upper sections, where bending moments are comparatively smaller than those at the base. Thus, the inclusion of the tower's torsional DOF is critical for accurately capturing the structural dynamics and load effects essential to design.

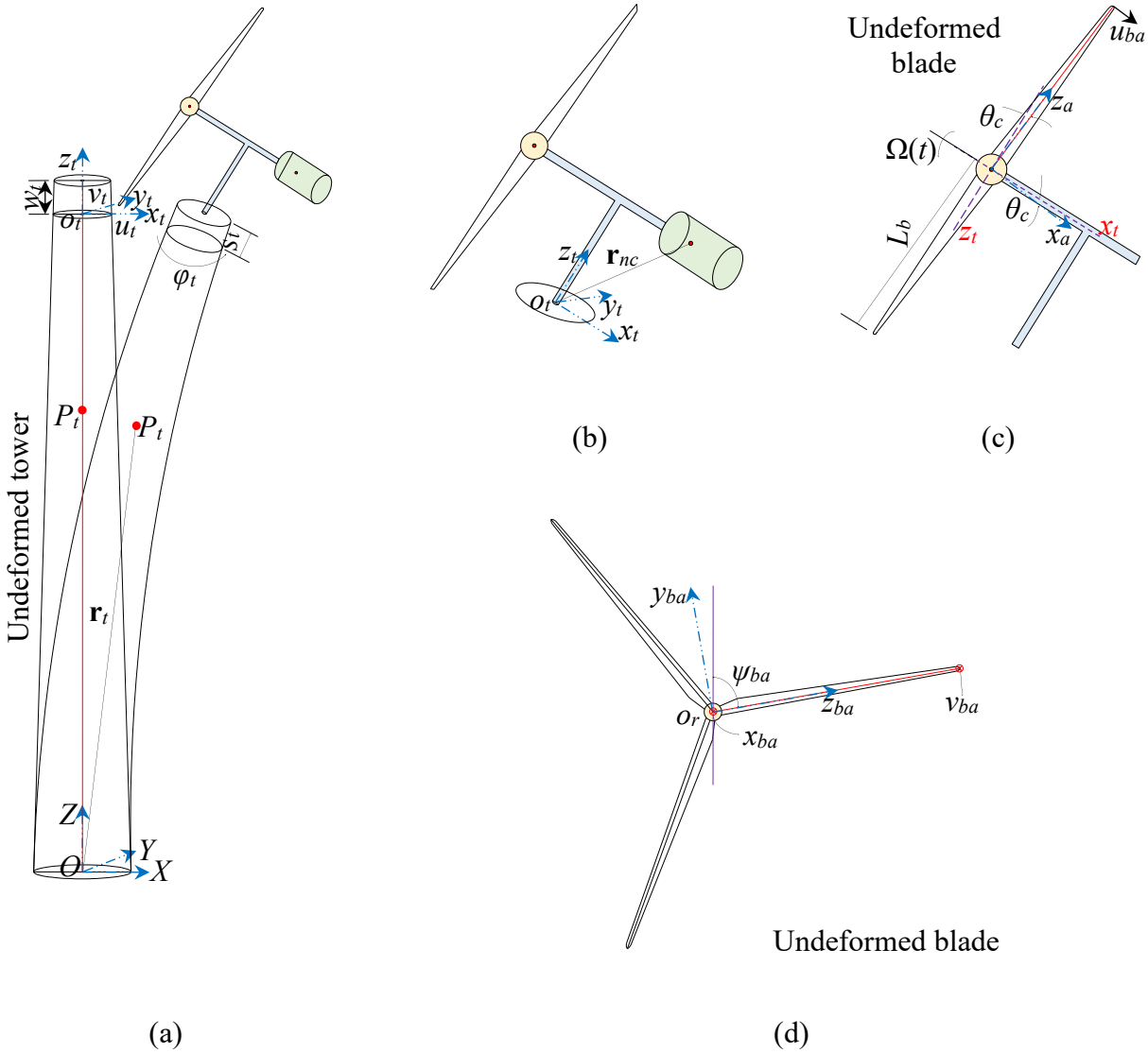

Figure 1. Schematic diagram of the OWT and each coordinate system. (a) Frame $\mathcal{F}_O$; (b) Frame $\mathcal{F}_T$; (c) Frame $\mathcal{F}_{ba}$-(Plane $o_h x_a z_a$); (d) Frame $\mathcal{F}_{ba}$ (Plane $o_h x_a y_a$).

The drivetrain, illustrated in Figure 2, is modeled based on St. Venant torsional theory using the DOFs $q_d(t)$ and $q_{dN}(t)$, which represent the angular deviations of the rotor and generator from their respective rated angular positions, $\Omega_0 t$ and $N_g \Omega_0 t$. Here, Ω_0 is the rated rotor speed, and N_g is the gearbox ratio. The actual rotor speed is expressed as $\Omega(t) = \Omega_0 + \dot{q}_d(t)$. The angular positions of the low- and high-speed shafts in the gearbox are denoted as $\theta_1(t)$ and $\theta_2(t)$, respectively. The gearbox and gear components are assumed to be rigid and massless, while the torsional stiffness coefficients k_{LSS} and

k_{HSS} of the low-speed shaft (LSS) and high-speed shaft (HSS) are derived from St. Venant torsional theory. Finally, the azimuthal angle of blade *a* relative to the nacelle is defined as:

$$\psi_{ba}(t) = \Omega_0 t + q_d(t) + \frac{2}{3}\pi(a-1) \quad a = 1,\ 2,\ 3 \tag{1}$$

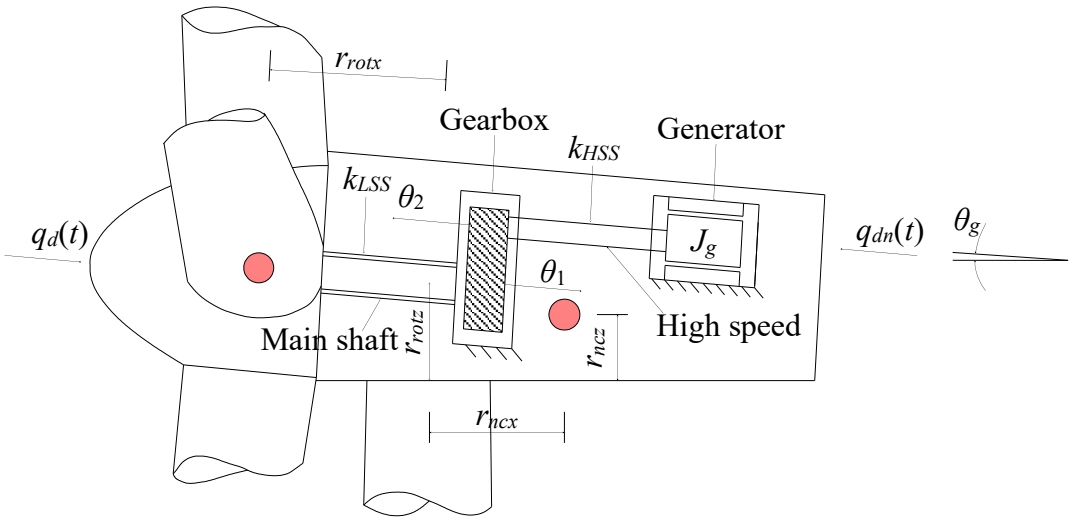

Figure 2. Schematic representation of a flexible drivetrain with a gearbox having an odd number of gear stages.

2.2. Tower kinetics model

The tower is modeled as a dynamic cantilever beam, where shear deformation and rotary inertia effects are neglected based on the slender beam assumption [17]. The deformation kinematics at an arbitrary point P_t along the beam are described using four field variables: the fore-aft displacement $u_t(z, t)$, side-side vibration $v_t(z, t)$, arc length stretch $s_t(z, t)$, and torsional angle $\varphi_t(z, t)$. The axial displacement $w_t(z, t)$ is dependent on the other three deformation variables and is expressed as [18]:

$$w_t \cong s_t - \frac{1}{2}\int_0^z [(\frac{\partial u_t}{\partial z})^2 + (\frac{\partial v_t}{\partial z})^2]dz \tag{2}$$

Given that axial stretch is negligible in typical tower dynamics (*i.e.*, $s_t = 0$), $w_t(z, t)$ can be formulated as:

$$w_t \cong -\frac{1}{2}\int_0^z [(\frac{\partial u_t}{\partial z})^2 + (\frac{\partial v_t}{\partial z})^2]dz \tag{3}$$

Thus, the position vector $\mathbf{r}_t$ and velocity vetor $\mathbf{v}_t$ of point P_t are respectively:

$$\mathbf{r}_t = [u_t\ v_t\ z + w_t]^T \tag{4}$$

$$\mathbf{v}_t = \dot{\mathbf{r}}_t = [\dot{u}_t\ \dot{v}_t\ \dot{w}_t]^T \tag{5}$$

Taking the time derivative of Equation (4), the expression for $\dot{w}_t$ is obtained as:

$$\dot{w}_t \cong -\int_0^z (\frac{\partial u_t}{\partial z}\frac{\partial^2 u_t}{\partial z \partial t} + \frac{\partial v_t}{\partial z}\frac{\partial^2 v_t}{\partial z \partial t})dz \tag{6}$$

The kinetic energy of the tower is then formulated as:

$$T_t = \frac{1}{2}\int_0^l m_t \mathbf{v}_t^T \mathbf{v}_t dz + \frac{1}{2}\int_0^l \rho_t J_{t\varphi} \dot{\varphi}_t^2 dz \tag{7}$$

where $m_t(z)$ is the mass per unit length of the tower (= $\rho_t A_t(z)$ with ρ_t and $A_t(z)$ being density and cross-section area at height z); l is the tower height; and $J_{t\varphi}(z)$ denotes the polar moment of inertia of the tower section.

The tower strain energy due to bending and torsional is written as:

$$V_{ts} = \frac{1}{2}\int_0^l E_t I_{ty} (\frac{\partial^2 u_t}{\partial z^2})^2 dz + \frac{1}{2}\int_0^l E_t I_{tx} (\frac{\partial^2 v_t}{\partial z^2})^2 dz + \frac{1}{2}\int_0^l G_t J_{t\varphi} (\frac{\partial \varphi_t}{\partial z})^2 dz \tag{8}$$

where E_t and G_t are the Young's modulus and shear modulus of the tower material, respectively; and $I_{tx}(z)$ and $I_{ty}(z)$ are the second moments of area about the local x- and y-axes, respectively.

The gravitational potential energy of the tower is given by:

$$V_{tg} = \int_0^l m_t g(\mathbf{r}_t^T \cdot \mathbf{K}) dz \tag{9}$$

where g is the gravitation acceleration; and $\mathbf{K} = [0\ 0\ 1]^T$ is the unit vector in the vertical direction. Thus, the total potential energy of the tower can be expressed as:

$$V_t = V_{ts} + V_{tg} \tag{10}$$

2.3. Nacelle model

Frame $\mathcal{F}_T$ is rigidly attached to the centroid of the tower tip cross-section and is initially aligned with the global inertial frame $\mathcal{F}_O$ in the undeformed configuration. The elastic rotation of the tower cross-section at the tip ($z = l$) is characterized by a second-order rotation tensor $\mathbf{R}_{el}$ [17,19]:

$$\mathbf{R}_{el} = \begin{bmatrix} 1-\frac{1}{2}(\frac{\partial u_t}{\partial z})^2 - \frac{1}{2}\varphi_t^2 & -\varphi_t - \frac{1}{2}\frac{\partial u_t}{\partial z}\frac{\partial v_t}{\partial z} & \frac{\partial u_t}{\partial z} \\ \varphi_t - \frac{1}{2}\frac{\partial u_t}{\partial z}\frac{\partial v_t}{\partial z} & 1-\frac{1}{2}(\frac{\partial v_t}{\partial z})^2 - \frac{1}{2}\varphi_t^2 & \frac{\partial v_t}{\partial z} \\ -\frac{\partial u_t}{\partial z} - \frac{\partial v_t}{\partial z}\varphi_t & -\frac{\partial v_t}{\partial z} + \frac{\partial u_t}{\partial z}\varphi_t & 1-\frac{1}{2}[(\frac{\partial u_t}{\partial z})^2 + (\frac{\partial v_t}{\partial z})^2] \end{bmatrix}_{z=l} \tag{11}$$

This formulation adequately captures the system's kinematic behavior under small-strain assumptions. The rotation matrix $\mathbf{R}_{el}$ serves to transform vectors from Frame $\mathcal{F}_T$ to Frame $\mathcal{F}_O$. Accordingly, the angular velocity of Frame $\mathcal{F}_T$ with respect to Frame $\mathcal{F}_O$, denoted by $\boldsymbol{\omega}_{tl}$, is computed as [20]:

$$\tilde{\boldsymbol{\omega}}_{tl} = \dot{\mathbf{R}}_{el} \mathbf{R}_{el}^T \tag{12}$$

where $\tilde{\boldsymbol{\omega}}_{tl}$ is the skew-symmetric matrix corresponding to the angular velocity vector $\boldsymbol{\omega}_{tl}$.

The displacement vector $\mathbf{r}_n$ and velocity vector $\mathbf{v}_n$ of the nacelle can be expressed as:

$$\mathbf{r}_n = \mathbf{r}_{tl} + \mathbf{R}_{el}\mathbf{r}_{nc} \tag{13}$$

$$\mathbf{v}_n = \dot{\mathbf{r}}_n = \mathbf{v}_{tl} + \dot{\mathbf{R}}_{el}\mathbf{r}_{nc} \tag{14}$$

where $\mathbf{r}_{tl}$ and $\mathbf{v}_{tl}$ is the displacement and velocity of the tower tip section center, respectively, *i.e.* $\mathbf{r}_{tl} = \mathbf{r}_t|_{z=l}$ and $\mathbf{v}_{tl} = \mathbf{v}_t|_{z=l}$.

The kinetic energy of the nacelle is:

$$T_n = \frac{1}{2} m_n \mathbf{v}_n^T \mathbf{v}_n + \frac{1}{2} \boldsymbol{\omega}_{tl}^T \mathbf{R}_{el} \mathbf{J}_n \mathbf{R}_{el}^T \boldsymbol{\omega}_{tl} \tag{15}$$

where m_n is the mass of the nacelle; and $\mathbf{J}_n$ is its mass moment of inertia matrices.

The gravitational potential energy of the nacelle is:

$$V_n = m_n g(\mathbf{r}_n^T \cdot \mathbf{K}) \tag{16}$$

2.4. Generator model

The coordinate transformation matrix from the rotor shaft coordinate system to Frame $\mathcal{F}_T$ is defined as:

$$\mathbf{R}_g = \begin{bmatrix} \cos\theta_g & 0 & \sin\theta_g \\ 0 & 1 & 0 \\ -\sin\theta_g & 0 & \cos\theta_g \end{bmatrix} \tag{17}$$

The kinetic and potential energy of the generator can be expressed as:

$$T_g = \frac{1}{2} \boldsymbol{\omega}_g^T \mathbf{R}_{el} \mathbf{R}_g \mathbf{J}_g (\mathbf{R}_{el} \mathbf{R}_g)^T \boldsymbol{\omega}_g \tag{18}$$

$$V_g = \frac{1}{2} k_{LSS} (\theta_1 - \Omega_0 t - q_d)^2 + \frac{1}{2} k_{HSS} (\theta_2 - N_g \Omega_0 t - q_{dn})^2 \tag{19}$$

where $\boldsymbol{J}_g$ is the mass moment of inertia tensor; and $\boldsymbol{\omega}_g$ is the angular velocity vector of the generator

$$\boldsymbol{\omega}_g = \boldsymbol{\omega}_{tl} + \mathbf{R}_{el} \mathbf{R}_g \begin{bmatrix} N_g \Omega_0 + \dot{q}_{dn} & 0 & 0 \end{bmatrix}^T \tag{20}$$

2.5. Rotor model

The displacement vector $\mathbf{r}_r$, velocity vector $\mathbf{v}_r$ and angular velocity vector vector $\boldsymbol{\omega}_r$ of the rotor can be expressed as:

$$\mathbf{r}_r = \mathbf{r}_{tl} + \mathbf{R}_{el} (\begin{bmatrix} 0 & 0 & r_{rotz} \end{bmatrix}^T + \mathbf{R}_g \begin{bmatrix} -r_{rotx} & 0 & 0 \end{bmatrix}^T) \tag{21}$$

$$\mathbf{v}_r = \dot{\mathbf{r}}_r = \mathbf{v}_{tl} + \dot{\mathbf{R}}_{el} (\begin{bmatrix} 0 & 0 & r_{rotz} \end{bmatrix}^T + \mathbf{R}_g \begin{bmatrix} -r_{rotx} & 0 & 0 \end{bmatrix}^T) \tag{22}$$

$$\boldsymbol{\omega}_r = \boldsymbol{\omega}_{tl} + \mathbf{R}_{el} \mathbf{R}_g \begin{bmatrix} \Omega_0 + \dot{q}_d & 0 & 0 \end{bmatrix}^T \tag{23}$$

The kinetic energy of the rotor is:

$$T_r = \frac{1}{2} m_r \mathbf{v}_r^T \mathbf{v}_r + \frac{1}{2} \boldsymbol{\omega}_r^T \mathbf{R}_{el} \mathbf{R}_g \mathbf{J}_r (\mathbf{R}_{el} \mathbf{R}_g)^T \boldsymbol{\omega}_r \tag{24}$$

where m_r is the mass of the rotor; and $\mathbf{J}_r$ is the mass moment of inertia tensor.

The gravitation potential energy of the rotor is:

$$V_r = m_r g(\mathbf{r}_r^T \cdot \mathbf{K}) \tag{25}$$

2.6. Blade kinetics model

The coordinate transformation matrix from the blade-local frame $\mathcal{F}_{ba}$ to the rotor shaft coordinate system is expressed as:

$$\mathbf{R}_{ba}=\begin{bmatrix}\cos\beta\cos\theta_c & \sin\beta\cos\theta_c & \sin\theta_c\\ \cos\beta\sin\theta_c\sin\psi_{ba}-\sin\beta\cos\psi_{ba} & \cos\beta\cos\psi_{ba}+\sin\beta\sin\theta_c\sin\psi_{ba} & -\cos\theta_c\sin\psi_{ba}\\ -\cos\beta\sin\theta_c\cos\psi_{ba}-\sin\beta\sin\psi_{ba} & \cos\beta\sin\psi_{ba}-\sin\beta\sin\theta_c\cos\psi_{ba} & \cos\theta_c\cos\psi_{ba}\end{bmatrix} \tag{26}$$

where θ_c is the pre-cone angle of the blade; and β is the collective blade pitch angle.

Following the same modeling strategy as the tower, the position vector $\mathbf{r}_{ba}$ and velocity vector $\mathbf{v}_{ba}$ of a point on blade a are expressed as:

$$\mathbf{r}_{ba}=\mathbf{r}_{tl}+\mathbf{R}_{el}\{[0\ 0\ r_{rotz}]^T+\mathbf{R}_g([-r_{rotx}\ 0\ 0]^T+\mathbf{R}_{ba}\mathbf{r}_b^a)\} \tag{27}$$

$$\begin{aligned}\mathbf{v}_{ba}=\dot{\mathbf{r}}_{ba}=\mathbf{v}_{tl}+\dot{\mathbf{R}}_{el}\{[0\ 0\ r_{rotz}]^T+\mathbf{R}_g([-r_{rotx}\ 0\ 0]^T+\mathbf{R}_{ba}\mathbf{r}_b^a)\}\\ +\mathbf{R}_{el}\{\dot{\mathbf{R}}_g([-r_{rotx}\ 0\ 0]^T+\mathbf{R}_{ba}\mathbf{r}_b^a)\}+\mathbf{R}_{el}\{\mathbf{R}_g(\dot{\mathbf{R}}_{ba}\mathbf{r}_b^a+\mathbf{R}_{ba}\dot{\mathbf{r}}_b^a)\}\end{aligned} \tag{28}$$

$$\mathbf{r}_b^a=[u_{ba}(r_b,\ t)\ v_{ba}(r_b,\ t)\ r_b]^T \tag{29}$$

$$\dot{\mathbf{r}}_b^a=[\dot{u}_{ba}\ \dot{v}_{ba}\ \dot{w}_{ba}]^T \tag{30}$$

The kinetic energy of the blade is:

$$T_b=\sum_{a=1}^{3}\frac{1}{2}\int_0^{L_b}m_b\mathbf{v}_{ba}^T\mathbf{v}_{ba}dr_b \tag{31}$$

where $m_b(r_b)$ is the mass per unit length of the blade; and L_b is the blade length.

The strain energy of the blade due to bending deformation is:

$$V_{bs}=\sum_{a=1}^{3}\frac{1}{2}\int_0^{L_b}E_bI_{by_a}(\frac{\partial^2u_{ba}}{\partial r_b^{\,2}})^2dr_b+\sum_{a=1}^{3}\frac{1}{2}\int_0^{L_b}E_bI_{bx_a}(\frac{\partial^2v_{ba}}{\partial r_b^{\,2}})^2dr_b \tag{32}$$

where E_b is the Young's modulus of the blade material; and I_{bx_a} and I_{by_b} are the cross-sectional moments of inertia in the flapwise and edgewise directions, respectively.

The centrifugal stiffening energy due to rotor rotation is:

$$\begin{aligned}V_{bcs}=\sum_{a=1}^{3}\frac{1}{2}\int_0^{L_b}[\int_{r_b}^{L_b}m_b(\Omega_0\cos\theta_c)^2r_bdr_b](\frac{\partial u_{ba}}{\partial r_b})^2dr_b\\ +\sum_{a=1}^{3}\frac{1}{2}\int_0^{L_b}[\int_{r_b}^{L_b}m_b(\Omega_0\cos\theta_c)^2r_bdr_b](\frac{\partial v_{ba}}{\partial r_b})^2dr_b\end{aligned} \tag{33}$$

The additional strain energy caused by gravitational loading during rotor rotation is:

$$\begin{aligned}V_{bgs}=-\sum_{a=1}^{3}\frac{1}{2}g\int_0^{L_b}[\int_{r_b}^{L_b}m_b(\cos\psi_{ba}\cos\theta_c\cos\theta_g-\sin\theta_c\sin\theta_g)dr_b](\frac{\partial u_{ba}}{\partial r_b})^2dr_b\\ -\sum_{a=1}^{3}\frac{1}{2}g\int_0^{L_b}[\int_{r_b}^{L_b}m_b(\cos\psi_{ba}\cos\theta_c\cos\theta_g-\sin\theta_c\sin\theta_g)dr_b](\frac{\partial v_{ba}}{\partial r_b})^2dr_b\end{aligned} \tag{34}$$

The gravitation potential energy of the blade is:

$$V_{bg}=\sum_{a=1}^{3}\int_0^{L_b}m_bg(\mathbf{r}_{ba}\cdot\mathbf{K})dr_b \tag{35}$$

Therefore, the total potential energy of blade is given by:

$$V_b = V_{bs} + V_{bg} + V_{bcs} + V_{bgs} \tag{36}$$

2.7. Spatial discretization method

The Assumed Mode Method (AMM) is employed to discretize the continuous deformation fields of the tower and blades, including $u_t(z, t)$, $v_t(z, t)$, $\varphi_t(z, t)$, $u_{ba}(r_b, t)$ and $v_{ba}(r_b, t)$ (a = 1, 2, 3). These fields are expanded using the following modal representations:

$$u_t(z,\ t) = \sum_{i=1}^{N_{tu}} \Phi_{ui}(z) T_{tui}(t) = \mathbf{\Phi}_u^T \mathbf{T}_{tu} \tag{37}$$

$$v_t(z,\ t) = \sum_{i=1}^{N_{tv}} \Phi_{vi}(z) T_{tvi}(t) = \mathbf{\Phi}_v^T \mathbf{T}_{tv} \tag{38}$$

$$\varphi_t(z,\ t) = \sum_{i=1}^{N_{t\varphi}} \eta_i(z) T_{t\varphi i}(t) = \boldsymbol{\eta}^T \mathbf{T}_{t\varphi} \tag{39}$$

$$u_{ba}(r_b,\ t) = \sum_{i=1}^{N_{bu}} \Psi_{ui}(r_b) T_{baui}(t) = \mathbf{\Psi}_u^T \mathbf{T}_{bau} \tag{40}$$

$$v_{ba}(r_b,\ t) = \sum_{i=1}^{N_{bv}} \Psi_{vi}(r_b) T_{bavi}(t) = \mathbf{\Psi}_v^T \mathbf{T}_{bav} \tag{41}$$

where $\Phi_{ui}(x)$, $\Phi_{vi}(x)$, $\eta_i(x)$, $\Psi_{ui}(r_b)$ and $\Psi_{vi}(r_b)$ are the assumed mode shape spatial functions. $\mathbf{\Phi}_u$, $\mathbf{\Phi}_v$, $\boldsymbol{\eta}$, $\mathbf{\Psi}_u$ and $\mathbf{\Psi}_v$ are the corresponding modal vectors. The numbers of mode shapes used for bending and twist discretization of the tower and blade are N_{tu}, N_{tv}, $N_{t\varphi}$, N_{bu}, and N_{uv} respectively. $T_{tui}(t)$, $T_{tvi}(t)$, $T_{t\varphi i}(t)$, $T_{baui}(t)$, and $T_{bavi}(t)$ (a = 1, 2, 3) are generalized coordinates to be determined. $\mathbf{T}_{tu}$, $\mathbf{T}_{tv}$, $\mathbf{T}_{t\varphi}$, $\mathbf{T}_{bau}$, and $\mathbf{T}_{bav}$ are the corresponding generalized coordinates vectors.

2.8. Formulating the equations of motion

A multibody-based formulation is adopted to derive the total kinetic and potential energies of the OWT system. The equations of motion are then obtained using the Euler-Lagrange equation [21,22]:

$$\frac{d}{dt}\left(\frac{\partial \mathcal{L}}{\partial \dot{\mathbf{q}}}\right) - \frac{\partial \mathcal{L}}{\partial \mathbf{q}} + \frac{\partial \Re}{\partial \dot{\mathbf{q}}} = \frac{\partial W_a}{\partial \mathbf{q}} \tag{42}$$

where $L = T - V$, with T and V being the system kinetic and potential energies, respectively; $\Re$ is the work performed by a nonconservative damping force; $\mathbf{q}(t)$ is the generalized coordinate vector corresponding to the 13 degrees of freedom; and W_a is the work induced by the aerodynamic load.

The total kinetic and potential energies of the system are given by:

$$T = T_t + T_n + T_g + T_r + T_b \tag{43}$$

$$V = V_t + V_n + V_g + V_r + V_b \tag{44}$$

The total nonconservative work $\Re$, due to structural and drivetrain damping, is composed of contributions from the tower, generator drivetrain, and blades:

$$\Re = \Re_t + \Re_g + \Re_b \tag{45}$$

$$\Re_t = \frac{1}{2}\int_0^l c_{tu} E_t I_{ty} (\frac{\partial^3 u_t}{\partial z^2 \partial t})^2 dz + \frac{1}{2}\int_0^l c_{tv} E_t I_{tx} (\frac{\partial^3 v_t}{\partial z^2 \partial t})^2 dz + \frac{1}{2}\int_0^l c_{t\varphi} G_t J_{t\varphi} (\frac{\partial^2 \varphi_t}{\partial z \partial t})^2 dz \quad (46)$$

$$\Re_g = c_{LSS}(\dot{\theta}_1 - \Omega_0 - \dot{q}_d)^2 + c_{HSS}(\dot{\theta}_2 - N_g\Omega_0 - \dot{q}_{dn})^2 \quad (47)$$

$$\Re_b = \sum_{a=1}^{3}\frac{1}{2}\int_0^{L_b} c_{bu} E_b I_{bya} (\frac{\partial^3 u_{ba}}{\partial r_b^2 \partial t})^2 dr_b + \sum_{a=1}^{3}\frac{1}{2}\int_0^{L_b} c_{bv} E_b I_{bxa} (\frac{\partial^3 v_{ba}}{\partial r_b^2 \partial t})^2 dr_b \quad (48)$$

where c_{LSS} and c_{HSS} are the of the damping coefficients of massless low speed shaft. c_{tu}, c_{tv} and $c_{t\varphi}$ are the damping coefficients associated with the two bending deformations and twist of the tower, respectively; and c_{bu} and c_{bv} are the damping coefficients associated with the two bending deformations of the blade. The coefficients can be calculated as

$$c_{tu} = 2\xi_t / \lambda_{tu},\ c_{tv} = 2\xi_t / \lambda_{tv},\ c_{t\varphi} = 2\xi_t / \lambda_{t\varphi} \quad (49)$$

$$c_{bu} = 2\xi_b / \lambda_{bu},\ c_{bv} = 2\xi_b / \lambda_{bv} \quad (50)$$

where ξ_t and ξ_b are the damping ratios of the tower and blade, respectively; λ_{tu}, λ_{tv}, and $\lambda_{t\varphi}$ are the fundamental natural frequencies (in rad/s) for the corresponding elastic deformations of the tower; and λ_{bu}, and λ_{bv} are the fundamental natural frequencies (in rad/s) for the corresponding elastic deformations of the blade.

3. Work by aerodynamic loads

Aerodynamic loads acting on both the blades and the tower are incorporated into the dynamic analysis of the wind turbine system. For the blades, the classical Blade Element Momentum (BEM) theory [4,5,23] is employed, augmented by three widely used correction models: Prandtl's tip loss factor, Glauert's turbulent wake correction, and the Pitt and Peters skewed wake model [24,25]. It is acknowledged that while BEM serves as an industry standard for integrated aero-servo-elastic simulations, several higher-fidelity modeling approaches exist for capturing more complex aerodynamic phenomena. These include Generalized Dynamic Wake Models [26], Free-Vortex Methods [27], and Computational Fluid Dynamics [28]. The selection of the enhanced BEM approach in this work is justified by its computational efficiency, which aligns with the objectives of the proposed intelligent analysis method. The exploration of higher-fidelity models like the Free-Vortex Method for specific complex scenarios is identified as a valuable direction for future research.

As illustrated in Figure 3, the distributed lift p_L, drag p_D and pitching moment M per unit span are determined from the 2D aerodynamic properties of the blade section. These loads are functions of the effective wind velocity V_{inf}, the relative inflow speed W, the angle of attack α and the local chord length c. The angle of attack is calculated by as the difference between the flow angle φ and the sum of the blade pitch angle β and the local blade pre-twist angle θ.

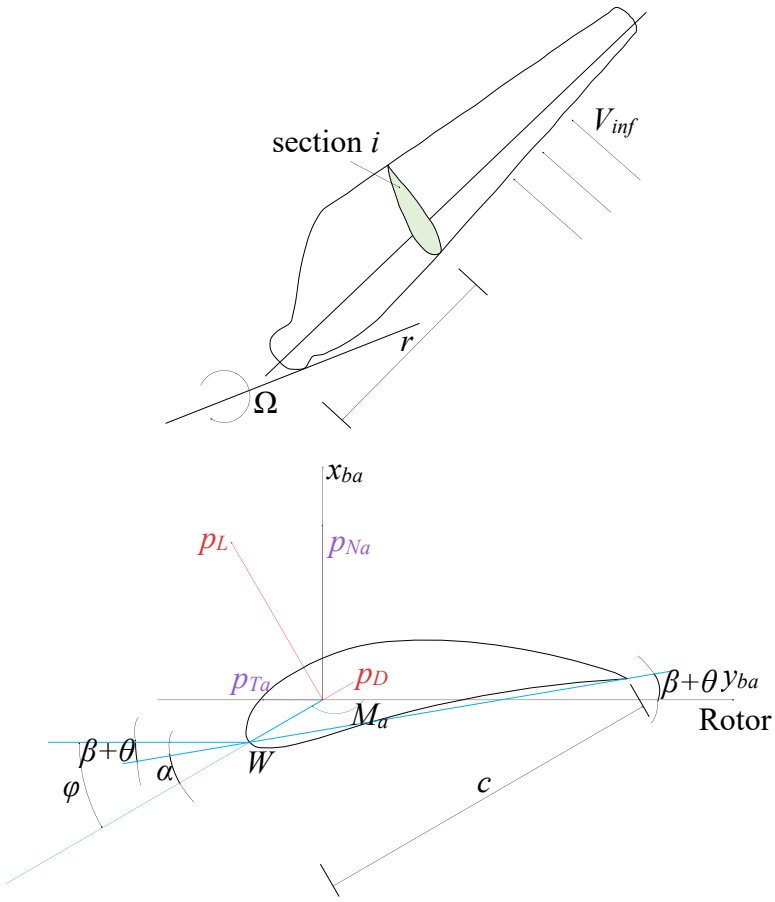

Figure 3. Illustration of the velocity triangle and force analysis for a blade element.

For the tower, aerodynamic loads are computed based on the quasi-steady assumption [29,30]. The distributed aerodynamic thrust (drag force) per unit length of the tower is expressed as:

$$\mathbf{p}_t = \frac{1}{2}\rho_a C_{dt} d_t \left|\mathbf{v}_w\right|^2 \tag{51}$$

where C_{dt} and d_t are the drag coefficient and diameter of the tower at height z; ρ_a is the density of air; and $\mathbf{v}_w$ is the incoming wind speed relative to the moving tower.

Based on the kinematic descriptions presented in Section 2, the total work done by the aerodynamic loads on the turbine system is be expressed as:

$$W_a = \sum_{a=1}^{3}\int_0^{L_b} \mathbf{p}_a^T \mathbf{r}_{bad} dr_b + \int_0^{l} \mathbf{p}_t^T \mathbf{r}_{td} dx \tag{52}$$

where $\mathbf{r}_{td}$ and $\mathbf{r}_{bad}$ are the displacement vector of tower and blade a, respectively.

4. Numerical simulation and validation

To derive the equations of motion capturing the complex kinematic behavior of the wind turbine system, a symbolic code was developed in MATLAB® based on the multibody formulation. The resulting system of nonlinear differential equations was numerically integrated using a stiff ordinary differential equation (ODE) solver in MATLAB® to compute the time-domain dynamic response.

A validation study was conducted to assess the reliability of the proposed model by comparing its predictions with those from OpenFAST, a widely recognized high-fidelity simulation tool in wind turbine dynamics research [31]. The benchmark configuration for this comparison was the 5 MW reference wind turbine developed by the National Renewable Energy Laboratory (NREL) [32].

Throughout the simulation, it was observed that the selection of vibration mode functions-specifically $\boldsymbol{\Phi}_u$, $\boldsymbol{\Phi}_v$, $\boldsymbol{\eta}$, for the tower, and $\boldsymbol{\Psi}_u$ and $\boldsymbol{\Psi}_v$ for the blades-plays a critical role in determining the accuracy of the computed dynamic response (see Figure 4 and Figure 5). These figures examine different first-order vibration mode functions to evaluate their impact on the structural response and to validate the suitability of the modal representations under various operating conditions.

$$\Phi_{u1}(z)=\Phi_{v1}(z)=\begin{cases}\frac{1}{3}(\frac{z}{l})^4-\frac{4}{3}(\frac{z}{l})^3+2(\frac{z}{l})^2 & \text{MF1}\\ 1-\cos\frac{z\pi}{2l} & \text{MF2}\\ \sin\frac{1.875z}{l}-1.3622\cos\frac{1.875z}{l}-\sinh\frac{1.875z}{l}+1.3622\cosh\frac{1.875z}{l} & \text{MF3}\end{cases} \tag{53}$$

$$\Psi_{ui}(r_b)=\Psi_{vi}(r_b)==\begin{cases}\frac{1}{3}(\frac{r_b}{L_b})^4-\frac{4}{3}(\frac{r_b}{L_b})^3+2(\frac{r_b}{L_b})^2 & \text{MF1}\\ 1-\cos\frac{r_b\pi}{2L_b} & \text{MF2}\\ \sin\frac{1.875r_b}{L_b}-1.3622\cos\frac{1.875r_b}{L_b}-\sinh\frac{1.875r_b}{L_b}+1.3622\cosh\frac{1.875r_b}{L_b} & \text{MF3}\end{cases} \tag{54}$$

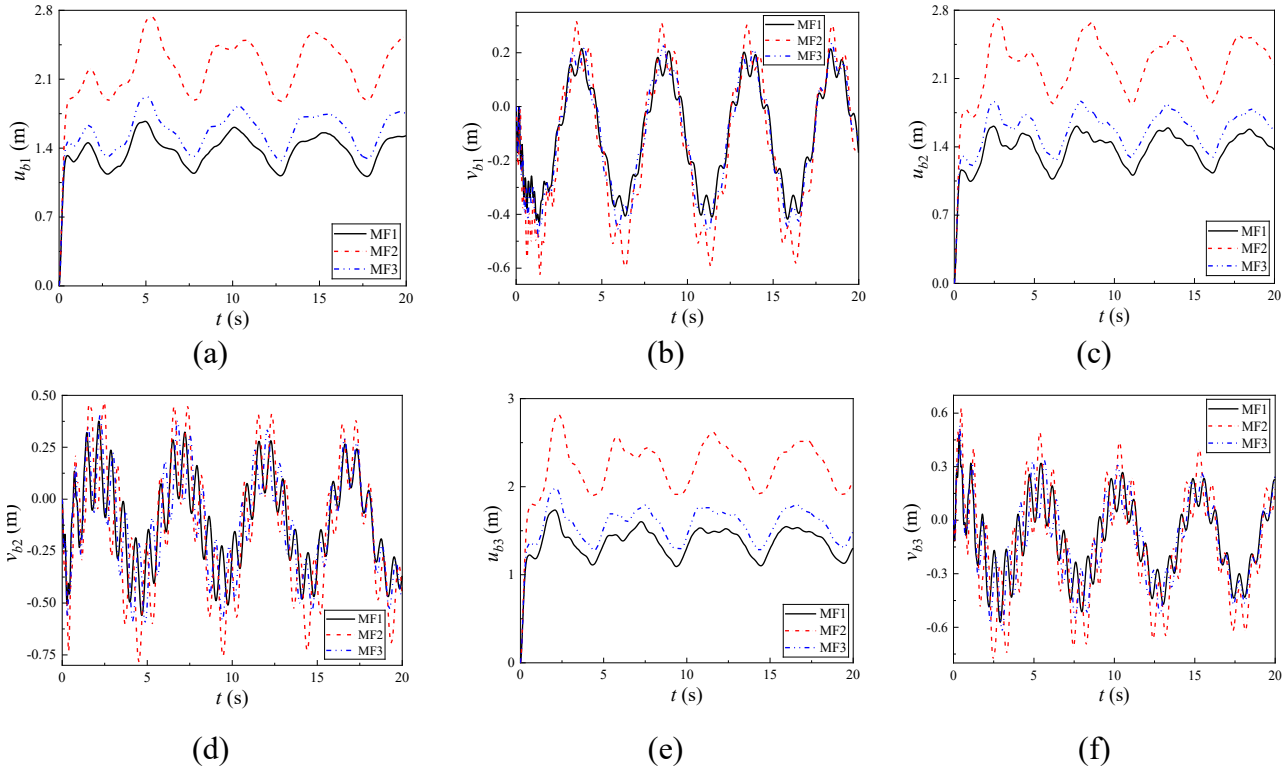

Figure 4. Comparison of dynamic responses obtained from different vibration mode functions (Blade). **(a)** Blade 1 (X direction); **(b)** Blade 1 (Y direction); **(c)** Blade 2 (X direction); **(d)** Blade 2 (Y direction); **(e)** Blade 3 (X direction); **(f)** Blade 3 (Y direction).

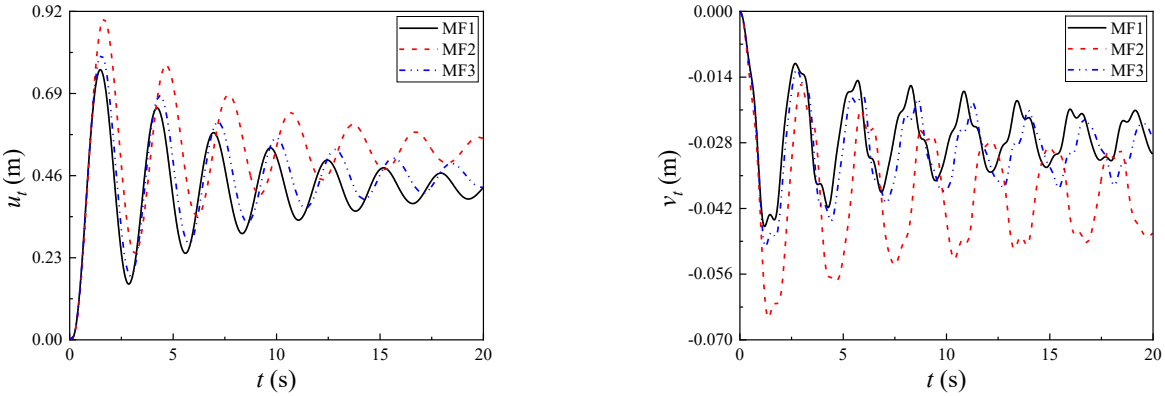

Figure 5. Comparison of dynamic responses obtained from different vibration mode functions (Tower). **(a)** X direction; **(b)** Y direction.

Building on the analyses in Figures 6–11, the modal expansions were extended from first four modes to first six modes (*i.e.* $N_{tt} = N_{tb} = N_{bb} = N_m = 4$–6), and the resulting simulations were compared with OpenFAST outputs. The comparison demonstrates that increasing the number of modal terms significantly improves the agreement between the presented method and OpenFAST results. However, this enhancement comes at the cost of increased computational effort, as the required calculation time grows proportionally with the number of modes (one hour to several hours). To achieve an optimal balance between computational efficiency and simulation accuracy, it is essential to adopt a differentiated modal expansion strategy-using tailored combination of modal terms for each variable, including u_t, v_t, u_{ba}, v_{ba} (a = 1, 2, 3).

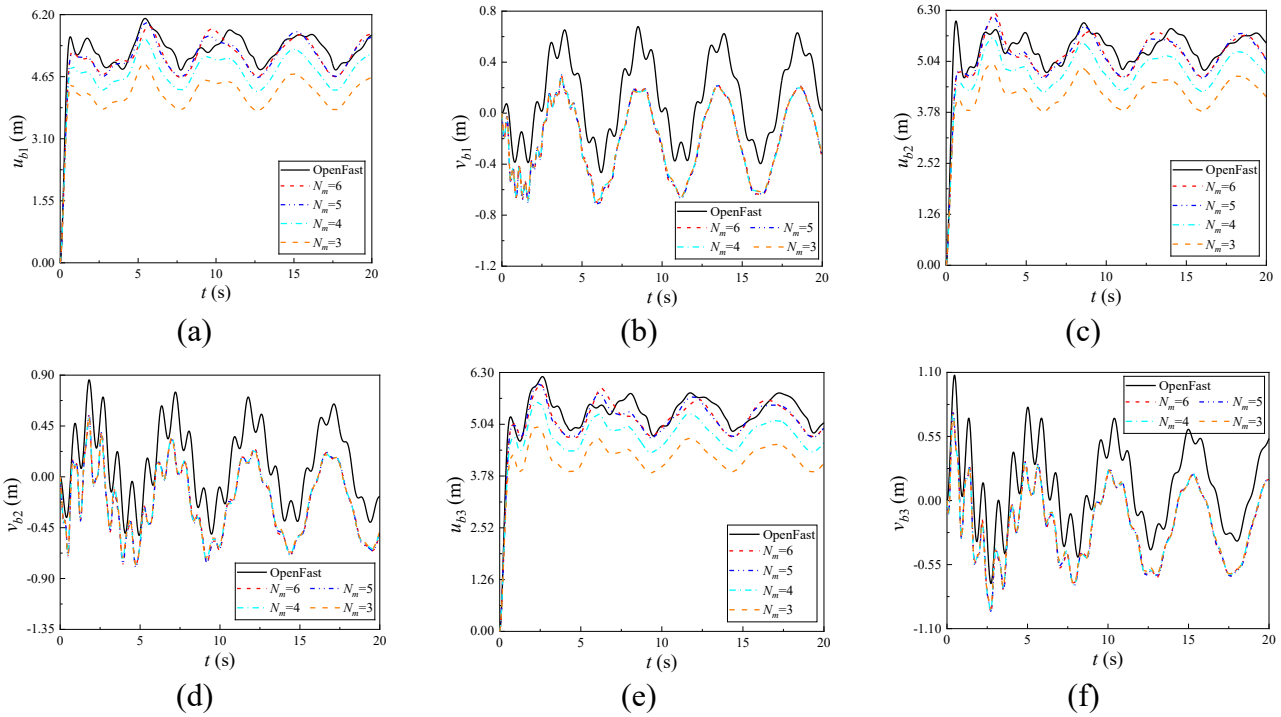

Figure 6. Comparison of blade tip displacement results (MF1). **(a)** Blade 1 (X direction); **(b)** Blade 1 (Y direction); **(c)** Blade 2 (X direction); **(d)** Blade 2 (Y direction); **(e)** Blade 3 (X direction); **(f)** Blade 3 (Y direction).

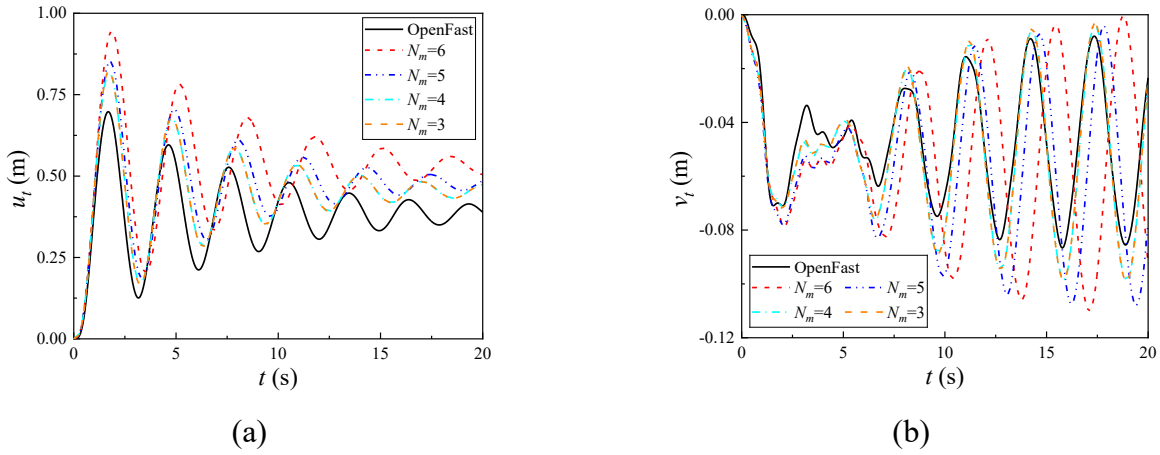

Figure 7. Comparison of tower tip displacement results (MF1). **(a)** X direction; **(b)** Y direction.

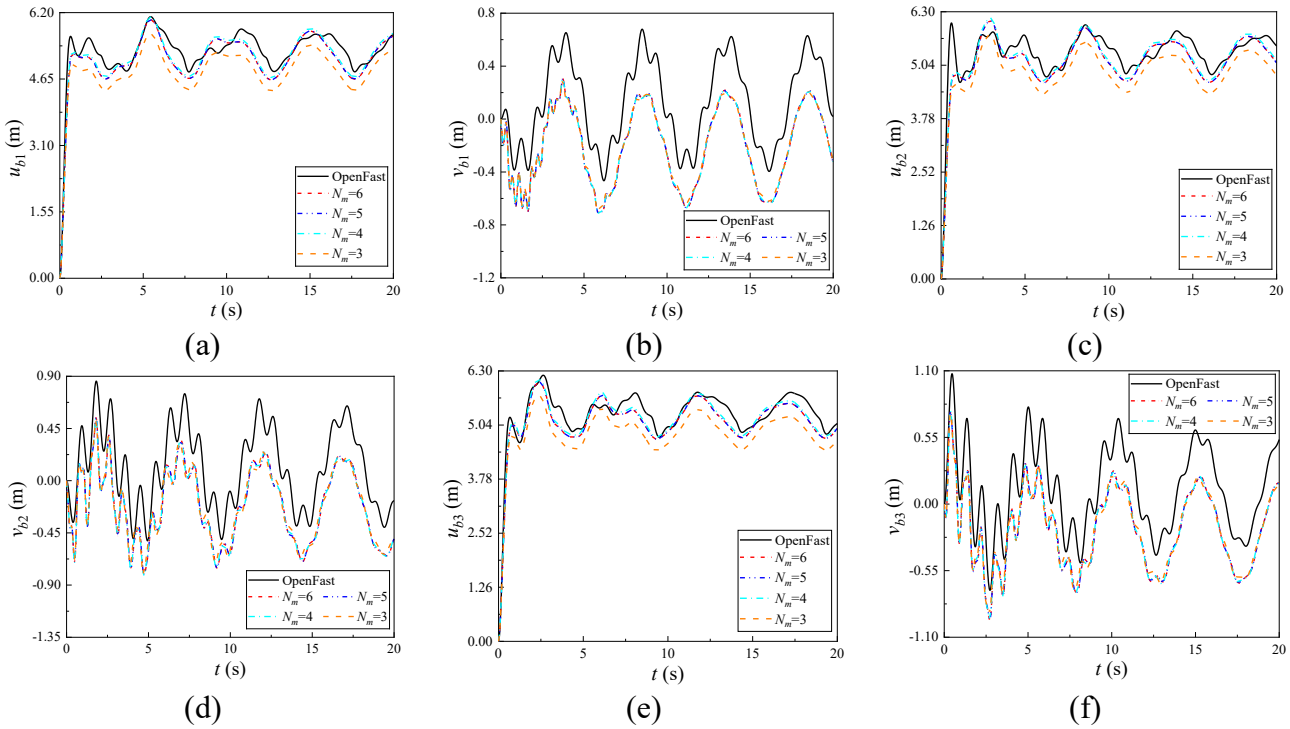

Figure 8. Comparison of blade tip displacement results (MF2). **(a)** Blade 1 (X direction); **(b)** Blade 1 (Y direction); **(c)** Blade 2 (X direction); **(d)** Blade 2 (Y direction); **(e)** Blade 3 (X direction); **(f)** Blade 3 (Y direction).

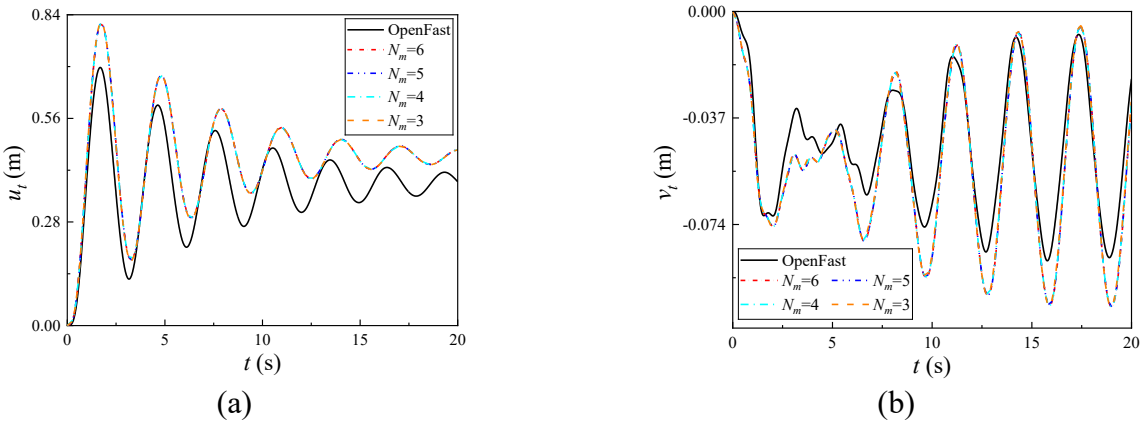

Figure 9. Comparison of tower tip displacement results (MF2). **(a)** X direction; **(b)** Y direction.

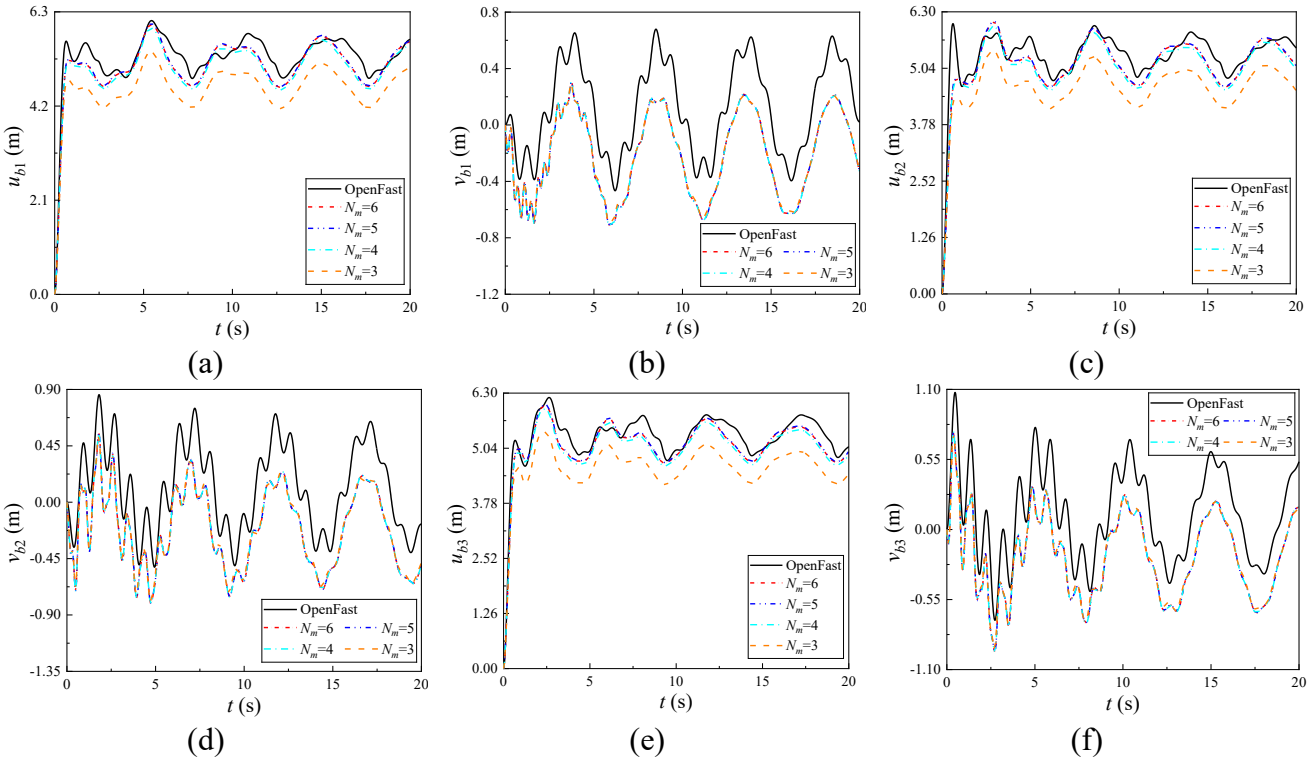

Figure 10. Comparison of blade tip displacement results (MF3). **(a)** Blade 1 (X direction); **(b)** Blade 1 (Y direction); **(c)** Blade 2 (X direction); **(d)** Blade 2 (Y direction); **(e)** Blade 3 (X direction); **(f)** Blade 3 (Y direction).

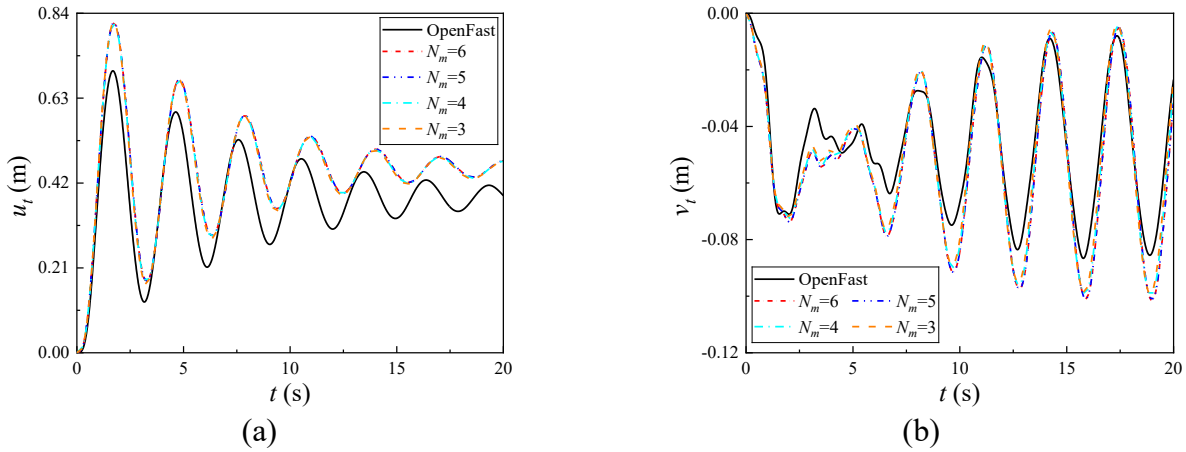

Figure 11. Comparison of tower tip displacement results (MF3). **(a)** X direction; **(b)** Y direction.

5. Intelligent analysis method

To achieve an optimal balance between computational efficiency (using an Intel(R) Core (TM) i7-11700 processor with 32.0 GB RAM). and response accuracy while accounting for the complexity and variability of structural vibration modes, an intelligent analysis algorithm [33,34] is proposed, as illustrated in Figure 12. It should be noted that the scope of this study does not extend to structural optimization; hence, the algorithm terminates once the modal function satisfying to the convergence criterion is identified.

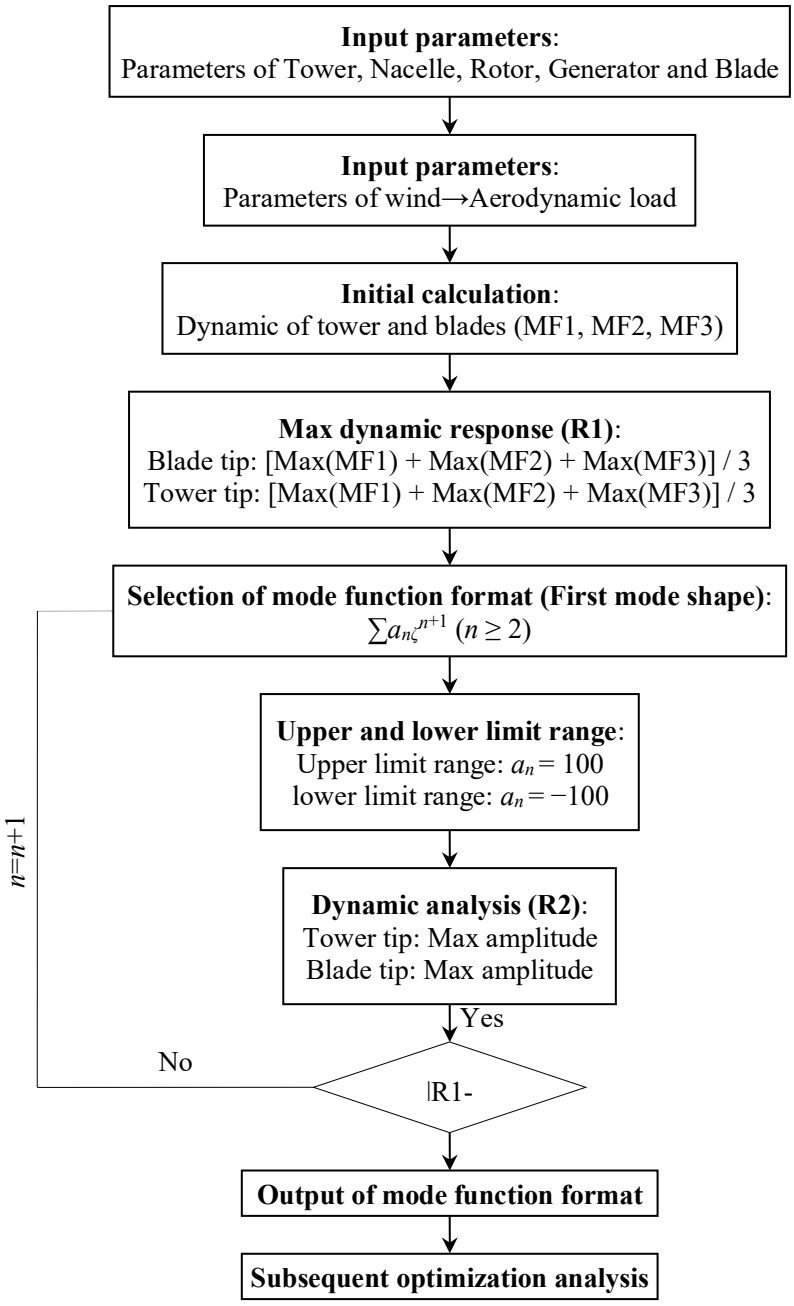

Figure 12. Flowchart of intelligent analysis algorithm.

Based on the modal formulations in Equations (53) and (54), along with the comparative results in Figure 4 and Figure 5, it is evident that appropriately relaxing the boundary conditions of the vibration modes can significantly improve the accuracy of dynamic response predictions. Here, the term "relaxation" does not imply a complete disregard for boundary constraints, but rather refers to an approximate satisfaction, which allows greater flexibility in mode shape representation without compromising physical relevance.

Figure 13 and Figure 14 compare the structural responses computed using the proposed intelligent algorithm with those from OpenFAST simulations. The results show that the relative error between the two approaches is within 3.5%, which falls within an acceptable range for engineering applications and confirms the effectiveness of the proposed method.

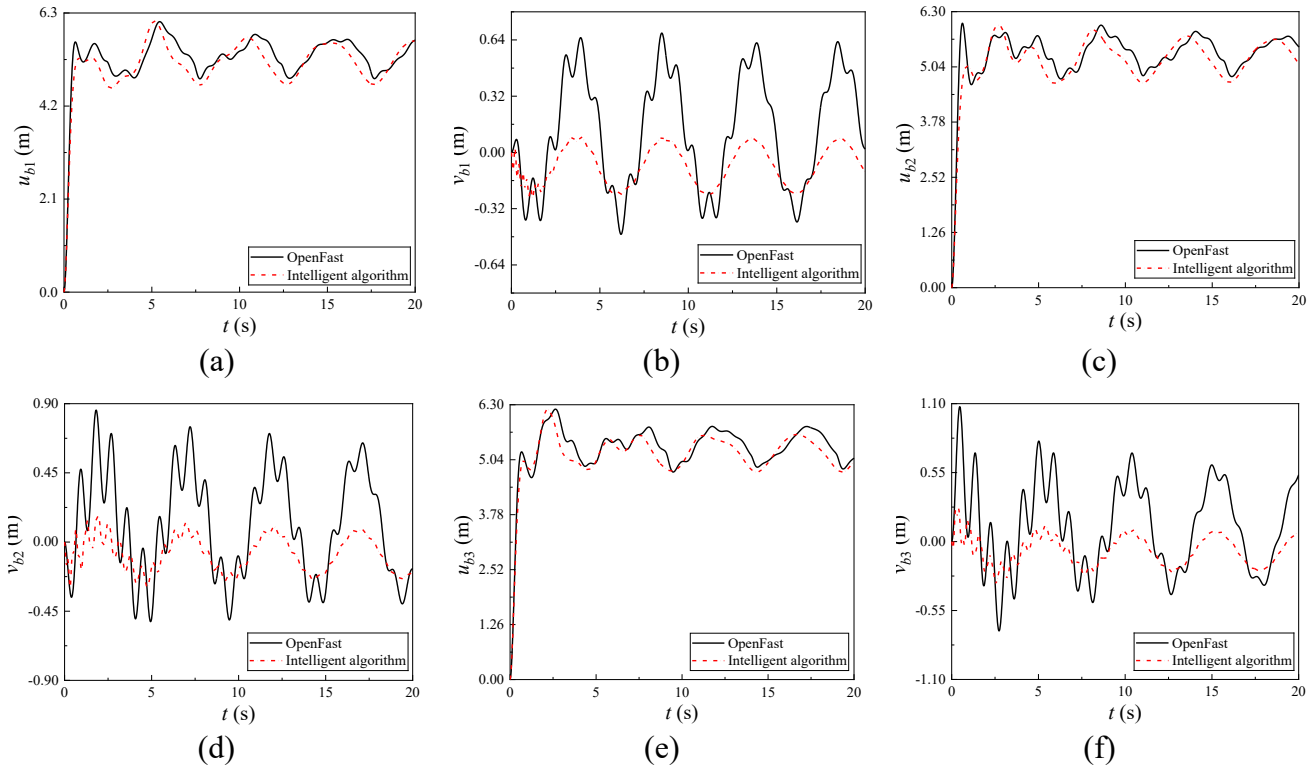

Figure 13. Comparison of blade tip displacement results (Intelligent algorithm). **(a)** Blade 1 (X direction); **(b)** Blade 1 (Y direction); **(c)** Blade 2 (X direction); **(d)** Blade 2 (Y direction); **(e)** Blade 3 (X direction); **(f)** Blade 3 (Y direction).

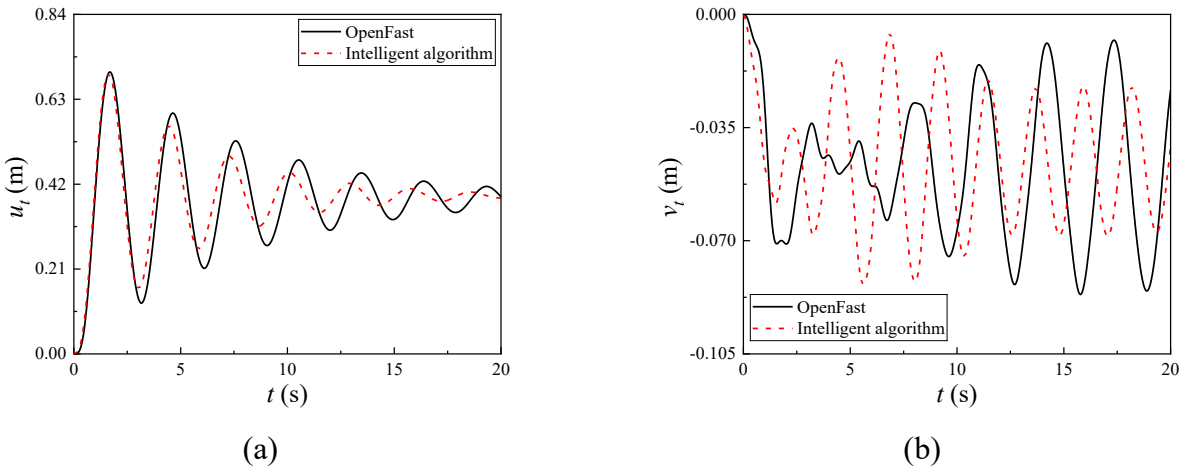

Figure 14. Comparison of tower tip displacement results (Intelligent algorithm). **(a)** X direction; **(b)** Y direction.

6. Conclusion

This study has established a comprehensive nonlinear dynamic modeling framework for onshore wind turbines using a 13-DOF multibody formulation derived from the Euler-Lagrange principle. The model effectively captures the fully coupled dynamics of the rotor-nacelle assembly and the supporting tower, with particular emphasis on the often-neglected torsional degree of freedom of the tower, which is critical for accurate load assessment in the upper tower sections. A key feature of the proposed framework is its integration of nonlinear aeroelastic blade response through modal decomposition and a

quasi-steady tower aerodynamics model, providing a physically consistent representation of the turbine behavior under operational conditions.

To address the critical challenge of balancing computational efficiency with simulation accuracy, an intelligent analysis algorithm was introduced for the optimal selection of vibration mode functions. Numerical validation against the high-fidelity OpenFAST code, using the NREL 5-MW reference turbine as a benchmark, confirmed the model's predictive capability under steady-state conditions. The results demonstrate that the proposed method achieves a close agreement with OpenFAST outputs, with relative errors maintained within 3.5%, while significantly reducing computational expense.

While the current model has demonstrated robust performance, this study also identifies key avenues for future theoretical enhancement and application broadening, directly informed by the review process:

- Towards Higher-Fidelity Dynamics: It is acknowledged that a more rigorous formulation of the generalized inertia matrix, explicitly accounting for Coriolis force effects and the contribution of tensor pairs, would further enhance the model's completeness and accuracy for regimes involving intense dynamic coupling. This constitutes a primary objective for deepening the theoretical foundation of this work.
- Expanding Operational Regimes: The successful validation under steady-state conditions provides a solid baseline for future investigations into more complex environments. Subsequent research will prioritize the analysis of non-steady-state conditions, such as responses under turbulent inflow and rapidly changing wind scenarios, which are crucial for predicting fatigue loads and optimizing control strategies in real-world applications.
- Extending Model Validation: To further corroborate the model's fidelity across a broader range of dynamic characteristics, future work will include a more comprehensive validation campaign. This will involve direct comparisons of fundamental natural frequencies and mode shapes with high-fidelity tools, as well as an analysis of local stress distributions under dynamic loading.

In summary, this work provides a robust and efficient simulation platform that balances accuracy with computational practicality, making it suitable for preliminary design, parameter sensitivity studies, and dynamic response analysis. The defined future directions, focused on enhancing theoretical rigor and expanding operational scope, chart a clear path for developing this framework into a high-fidelity tool for the next generation of wind turbine systems.

Acknowledgments

The authors are grateful for the financial support provided by the National Natural Science Foundation of China (Grant No. 52278175), and the Fundamental Research Funds for the Central Universities (Grant No. 531118010784).

Authors' contribution

Conceptualization, Xuhong Zhou, Jiepeng Liu, Guoqing Huang and Liang Cao; methodology, Liang Cao and Maolin Dai; software, Maolin Dai and Liang Cao; validation, Liang Cao, Maolin Dai and Guoqing Huang; formal analysis, Liang Cao; investigation, Maolin Dai; resources, Liang Cao; data curation, Liang Cao; writing—original draft preparation, Maolin Dai; writing—review and editing, Liang Cao; visualization, Liang Cao; supervision, Liang Cao; project administration, Liang Cao; funding acquisition, Liang Cao. All authors have read and agreed to the published version of the manuscript.

Conflicts of interests

Jiepeng Liu holds the position of Associate Editor-in-Chief for *Smart Construction* and has not peer reviewed or made any editorial decisions for this paper.

References

[1] Li H, Wang S, Jiang J, Liu J, Ou J, *et al*. Preserving normal power curve data with sparse density via wind speed-power correlation trend cleaning method. *IEEE Trans*. *Sustain*. *Energy* 2025, 16(1):365–376.

[2] Wang Z, Qin Y, Lin X, Li X,·Wang L, *et al*. Vibration suppression and dynamical bifurcation of aeolian vibration for the transmission conductor based on nonlinear energy sink. *Nonlinear Dyn*. 2025, 113(1):28733–28755.

[3] Global Wind Energy Council. Available: https://www.gwec.net/reports/globaloffshorewindreport (accessed on 25 June 2025).

[4] Prasad CS, Dimitriadis G. Application of a 3D unsteady surface panel method with flow separation model to horizontal axis wind turbines. *J. Wind Eng. Ind. Aerodyn*. 2017, 166:74–89.

[5] Prasad CS, Chen QZ, Bruls O, D'Ambrosio F, Dimitriadis G. Aeroservoelastic simulations for horizontal axis wind turbines. *Proc. Inst. Mech. Eng., Part A: J. Power Energy* 2017, 231(2):103–117.

[6] Al-Sanad S, Parol J, Wang L, Kolios A. Structural optimisation framework for onshore wind turbine towers considering multiple design constraints. *Int. J. Sustain. Energy* 2022, 41(5):469–491.

[7] Fernández-Escobar CJ, Vega-Posada CA, Garcia-Aristizábal EF. Lateral deformation and buckling analysis of piles including shear effects: numerical analysis. *Eng. Struct.* 2023, 277:115416.

[8] Diken H, Asiri S. Vibration analysis of horizontal axis wind turbine considering tower-nacelle-foundation interaction. *J. Vib. Eng. Technol.* 2024, 12(2):1849–1860.

[9] Quilligan A, O'Connor A, Pakrashi V. Fragility analysis of steel and concrete wind turbine towers. *Eng. Struct.* 2012, 36:270–282.

[10] Zhao L, Mbachu J, Liu S, Zhang R. Working status prediction for a high-formwork support system using finite element model-informed deep learning model and GPT-aided method. *Smart Constr.* 2025, 2(2):0015.

[11] Liu Y, Wang Y, Zhou X, Ren W, Zhang F, *et al*. Lateral bearing capacity of self-centering prestressed concrete filled steel tubular lattice rocking tower. *J. Constr. Steel. Res.* 2025, 231:109616.

[12] Wang D, Xu J, He Z, Yu Q, Tang W, *et al*. High-fidelity integrated co-simulation model for dynamic analysis of onshore wind turbines with steel-concrete hybrid tower. *Mech. Syst. Signal Proc.* 2025, 230:112583.

[13] Park KP, Cha JH, Ku N. The flexible multibody dynamics of a floating offshore wind turbine in marine operations. *Ships Offshore Struct.* 2017, 12(4):563–574.

[14] Liu Y, Xiao Q, Incecik A, Peyrard C. Aeroelastic analysis of a floating offshore wind turbine in platform-induced surge motion using a fully coupled CFD-MBD method. *Wind Energy* 2019, 22(1):1–20.

[15] Al-Solihat MK, Nahon M, Behdinan K. Dynamic modeling and simulation of a spar floating offshore wind turbine with consideration of the rotor speed variations. *J. Dyn. Syst. Meas. Contr.* 2019, 141(8):081014.

[16] Prasad CS, Kolman R, Pesek L. Meshfree reduced order model for turbomachinery blade flutter analysis. *Int. J. Mech. Sci.* 2022, 222:107222.
[17] Al-Solihat MK, Nahon M. Flexible multibody dynamic modeling of a floating wind turbine. *Int. J. Mech. Sci.* 2018, 142:518–529.
[18] Yoo HH, Ryan RR, Scott RA. Dynamics of flexible beams undergoing overall motions. *J. Sound Vib.* 1995, 181(2):261–278.
[19] Shi P, McPhee J, Heppler GR. A deformation field for Euler-Bernoulli beams with applications to flexible multibody dynamics. *Multibody Syst. Dyn.* 2001, 5(1):79–104.
[20] Haug EJ. Computer-aided kinematics and dynamics of mechanical systems, 1st ed. Boston: Allyn and Bacon, 1989.
[21] Peng RL, Guo R, Ji J, Zheng B, Miao Z, *et al*. Neural network-based task-space bipartite region reaching control for heterogeneous networked Euler-Lagrange systems. *Nonlinear Dyn.* 2025, 113(20):27769–27784.
[22] Srinivas T, Tomar G. A generalized correction scheme for two-way coupled particle-laden Euler-Lagrange simulations. *Comput. Fluids* 2025, 290:106554.
[23] Yin J, Shen W, Sun Z, Zhu W, Cho HS. A new Blade Element Momentum theory for both compressible and incompressible wind turbine flow computations. *Energy Convers. Manag.* 2025, 328:119619.
[24] Branlard E, Dixon K, Gaunaa M. Vortex methods to answer the need for improved understanding and modelling of tip-loss factors. *IET Renew. Power Gener.* 2013, 7(4):311–320.
[25] Høeg CE, Zhang Z. The influence of gyroscopic effects on dynamic responses of floating offshore wind turbines in idling and operational conditions. *Ocean Eng.* 2021, 227:108712.
[26] Jeon M, Lee S, Kim T, Lee S. Wake influence on dynamic load characteristics of offshore floating wind turbines. *AIAA J.* 2016, 54(11):3535–3545.
[27] Bagai A, Leishman JG, Park J. Aerodynamic analysis of a helicopter in steady maneuvering flight using a free-vortex rotor wake model. *J. Am. Helicopter Soc.* 1999, 44(2):109–120.
[28]Biswas R, Strawn RC. Tetrahedral and hexahedral mesh adaptation for CFD problems. *Appl. Numer. Math.* 1998, 26(1–2):135–151.
[29] Liu Z, Song Y, Chen J. Coupled rigid-flexible dynamics modeling and validations of floating offshore wind turbine. *Ocean Eng.* 2023, 267:113200.
[30] Senjanovi I, Tomi M, Hadi N. Formulation of consistent nonlinear restoring stiffness for dynamic analysis of tension leg platform and its influence on response. *Mar. Struct.* 2013, 30:1–32.
[31] Ghozlane M, Najar F. Nonlinear analysis of a floating offshore wind turbine with internal resonances. *Nonlinear Dyn.* 2024, 112(3):1729–1757.
[32] Jonkman J, Butterfield S, Musial W, Scott G. Definition of 5-MW reference wind turbine for offshore system development. 2009. Available: https://docs.nrel.gov/docs/fy09osti/38060.pdf (accessed on 10 February 2009).
[33] Guo X, Huang Y, Ma G. Recent research developments in intelligent methodologies for prefabricated construction. *Smart Constr.* 2024, 2(1):0007.
[34] Brugnoli A, Matignon D, Morlier J. A linearly-implicit energy-momentum preserving scheme for geometrically nonlinear mechanics based on non-canonical Hamiltonian formulations. *Nonlinear Dyn.* 2025, 113(20):27539–27566.